nature COMMUNICATIONS

ARTICLE

DOI: 10.1038/s41467-017-01811-x OPEN

Structurally triggered metal-insulator transition in rare-earth nickelates

Alain Mercy[1], Jordan Bieder[1,2], Jorge Íñiguez[3] & Philippe Ghosez[1]

Rare-earth nickelates form an intriguing series of correlated perovskite oxides. Apart from $LaNiO_3$, they exhibit on cooling a sharp metal-insulator electronic phase transition, a concurrent structural phase transition, and a magnetic phase transition toward an unusual antiferromagnetic spin order. Appealing for various applications, full exploitation of these compounds is still hampered by the lack of global understanding of the interplay between their electronic, structural, and magnetic properties. Here we show from first-principles calculations that the metal-insulator transition of nickelates arises from the softening of an oxygen-breathing distortion, structurally triggered by oxygen-octahedra rotation motions. The origin of such a rare triggered mechanism is traced back in their electronic and magnetic properties, providing a united picture. We further develop a Landau model accounting for the metal-insulator transition evolution in terms of the rare-earth cations and rationalizing how to tune this transition by acting on oxygen rotation motions.

[1] Theoretical Materials Physics, Q-MAT, CESAM, University of Liège, B-4000 Liège, Belgium. [2] CEA DAM-DIF, F-91297 Arpajon, France. [3] Materials Research and Technology Department, Luxembourg Institute of Science and Technology (LIST), 5 avenue des Hauts-Fourneaux, L-4362 Esch/Alzette, Luxembourg. Correspondence and requests for materials should be addressed to P.G. (email: philippe.ghosez@ulg.ac.be)

First synthesized in 1971[1], rare-earth nickelates ($RNiO_3$, with R = rare earth) are appealing for various applications[2, 3], and the possibility to tune their properties in epitaxial films and heterostructures[4] has recently fueled an even larger interest[5–7]. $RNiO_3$ compounds belong to the family of perovskite oxides with a reference $Pm\bar{3}m$ cubic structure (Fig. 1a), nevertheless not directly observed. Apart for $LaNiO_3$, which always keeps a metallic $R\bar{3}c$ phase and will not be further discussed here, all $RNiO_3$ adopt at reasonably high temperature a metallic $Pbnm$ orthorhombic phase[8]. This phase, rather ubiquitous[9] amongst perovskites with small Goldschmidt tolerance factor[8], t, corresponds to a distortion of the cubic structure arising from the appearance of combined anti-phase rotations of the oxygen octahedra along the x and y directions, R_{xy} (Fig. 1b), with the same amplitude Q_R and in-phase rotations of the oxygen octahedra along z, M_z (Fig. 1c), with amplitude Q_M.

In this phase, all Ni atoms are equivalent and formally in a Jahn-Teller active d^7 (likely $t_{2g}^6 e_g^1$ low spin) configuration. Surprisingly, although compatible with the $Pbnm$ symmetry, cooperative Jahn-Teller distortions do not appear. Instead, at a temperature T_{MI}, which strongly evolves with the R cation (i.e., with t)[10], $RNiO_3$ compounds exhibit an electronic metal-insulator transition (MIT), which was shown to be concurrent with a structural transition from $Pbnm$ to monoclinic $P2_1/n$ symmetry[11]. This symmetry lowering is accompanied with the appearance of a breathing distortion of the oxygen octahedra, B_{OC} (Fig. 1d), which alternatively expand and contract with amplitude Q_B, according to a rock-salt pattern. This gives rise to two types of Ni sites with long and short Ni–O bonds, respectively.

At low temperature (100–200 K), $RNiO_3$ compounds finally show a magnetic phase transition toward an unusual E′-type antiferromagnetic (AFM) spin order identified by a Bragg vector $\mathbf{q} = (1/4, 1/4, 1/4)$ in pseudocubic notation[11–13]. For large cations (R = Nd and Pr), the Néel temperature $T_N = T_{MI}$ and the system goes directly from paramagnetic metal (PM-M) to AFM insulator (AFM-I). For smaller R cations, T_N is much lower than T_{MI}; the two phase transitions are decoupled and the system goes through an intermediate paramagnetic insulating phase (PM-I).

The origin of the MIT has been widely debated in the literature[14–19]. It was sometimes interpreted as a charge disproportionation at Ni sites[20]: $2(d^7) \rightarrow d^8 + d^6$. However, the importance of Ni 3d-O 2p hybridization—i.e., transfer of electrons from O to Ni and formation of oxygen holes ($\underline{L}$) keeping Ni in a d^8 configuration (i.e., $d^{8-n} \approx d^8\underline{L}^n$)—was evoked early on[15]. Nowadays, the MIT is usually viewed as a charge ordering of the type $2(d^8\underline{L}^1) \rightarrow (d^8) + (d^8\underline{L}^2)$[17, 21, 22]. In this scenario, B_{OC} appears important to stabilize the charge ordering and open the gap. As suggested in ref. [23] and confirmed from statistical correlation techniques[24], R_{xy} and M_z are also expected to play an active role. However, a complete picture linking electronic, structural and magnetic properties is yet to emerge.

Unlike recent theoretical studies, which were focusing specifically on the electronic properties[17–19, 21], we investigate here self-consistently the electronic and structural degrees of freedom of $RNiO_3$ compounds from density functional theory calculations (DFT, see Methods). Specific care was given to the validation of our approach, which turns out to provide an unprecedented agreement with experimental data. Focusing on $YNiO_3$, we show (Supplementary Notes 1–4) that not only the atomic structure but also the AFM-E′ ground state, the estimated T_N and the electronic bandgap of the insulating phase are very accurately reproduced, making therefore our approach a method of choice to shed light on the interlink between these different features.

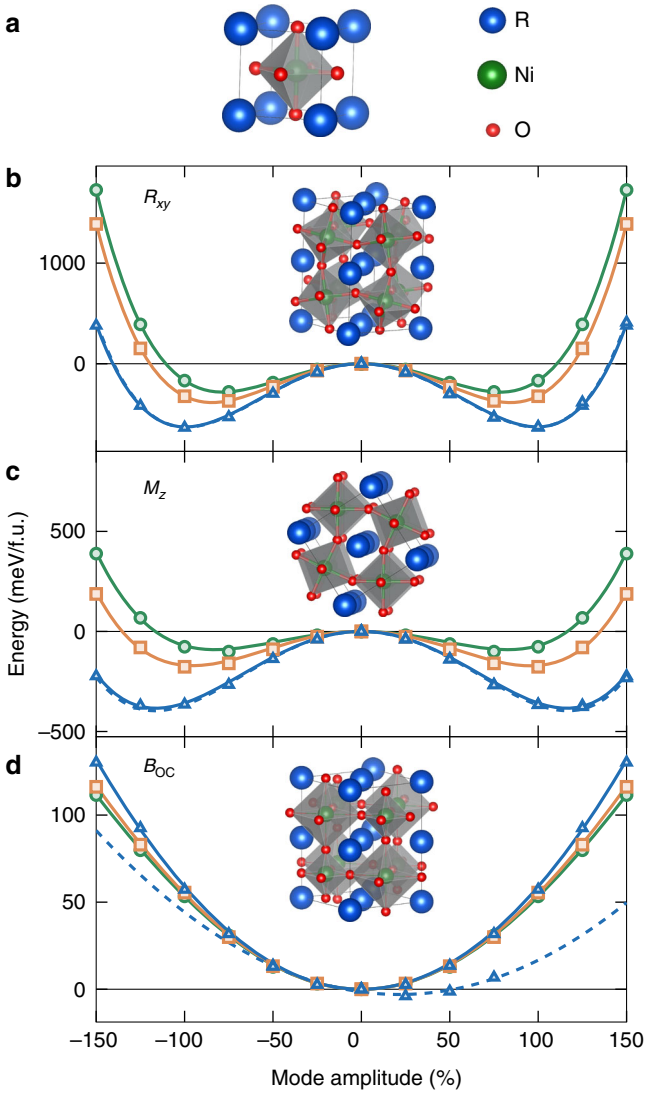

Fig. 1 Reference cubic perovskite structure and most relevant atomic distortions. **a** Sketch of the reference $Pm\bar{3}m$ cubic perovskite cell of $RNiO_3$ compound with R at the corner, Ni at the center, and O atoms at the middle of the faces, forming corner-shared octahedra surrounding the B atoms. Starting from this reference, three main atomic distortions drive the system successively to the $Pbnm$ and then $P2_1/n$ phases: **b** anti-phase rotations of oxygen octahedra of same amplitudes about x- and y-axis (R_{xy}), **c** in-phase rotations of oxygen octahedra about z-axis (M_z), **d** breathing of the oxygen octahedra (B_{OC}). The energy wells associated to the freezing of individual distortion of increasing amplitude in the cubic cell are shown for different R cations, associated to distinct tolerance factor t, and either a ferromagnetic (full line) or E′-type antiferromagnetic (dashed line, only for R = Y) spin arrangement: $YNiO_3$ ($t = 0.920$, blue); $GdNiO_3$ ($t = 0.938$, orange) and $SmNiO_3$ ($t = 0.947$, green). The atomic distortions are normalized to their amplitude in the $P2_1/n$ AFM-E′ ground state of $YNiO_3$. Calculations are done for each compound in a cubic cell that has the same volume as the ground state

Results

Energetics of individual lattice distortions. We start from the reference $Pm\bar{3}m$ cubic structure. Inspection of the phonon dispersion curves (Supplementary Note 5) reveals dominant structural instabilities at R ($\omega_R = 310i\ cm^{-1}$) and M ($\omega_M = 278i\ cm^{-1}$) points of the Brillouin zone (BZ), which are associated, respectively, to the R_{xy} and M_z distortions responsible for the $Pbnm$ phase. These imaginary frequencies ω_i are linked to a negative

energy curvature α_i at the origin $(\alpha_i \propto \omega_i^2 < 0)$ and to a typical double-well (DW) shape of the energy when freezing R_{xy} and M_z distortions of increasing amplitude within the cubic structure, as illustrated in Fig. 1. These wells are nearly independent of the spin order but strongly evolve with the R cation: they become shallower when R size increases, consistently with a reduction of the related distortion amplitudes in the *Pbnm* phase.

In contrast, the B_{OC} motion, corresponding to another phonon at R, is stable and extremely stiff (in fact the stiffest mode with $\omega_B = 700\ cm^{-1}$), in line with the single-well (SW) shape illustrated in Fig. 1. Decreasing R cation size tends to stabilize slightly further B_{OC}, in apparent contradiction with the observed increase of T_{MI}. As illustrated for $YNiO_3$, switching from ferromagnetic (FM) to AFM-E′ spin order reduces slightly the curvature but does not reverse it; instead it shifts the SW to lower energy[13], yielding a finite Q_B at the minimum. Although B_{OC} tends to make the system insulating, this amplitude (25% of ground state's value) is however not large enough to open a gap (more than 75% would be required). This shows that B_{OC} and the magnetic order alone cannot explain the MIT by themselves.

Mode coupling and triggered mechanism. Our central result is presented in Fig. 2 where we report in panel a the evolution of the B_{OC} energy well of $YNiO_3$ at various fixed amplitudes of oxygen rotation motions. It highlights that although initially stable (SW), B_{OC} is progressively destabilized (DW) by the appearance of R_{xy} and M_z. As illustrated in panel b, α_B is renormalized into $\tilde{\alpha}_B$, which evolves linearly with Q_R^2 and Q_M^2. The slope associated to Q_R is twice as large as that related to Q_M, attesting that each of the three individual rotations similarly affects B_{OC}. This behavior arises from the presence in the energy expansion of cooperative $(\lambda < 0)$ bi-quadratic coupling terms between B_{OC} and oxygen rotations ($E \approx \lambda_{Bi} Q_B^2 Q_i^2$, i = M,R), which, being the lowest-order couplings allowed by symmetry, should give rise to the appearance of B_{OC} through a triggered phase transition according to Holakovsky[25]. The same behavior is observed independently of the magnetic order (Supplementary Note 8). From now we focus on representative FM results while coming back to the role of magnetism later.

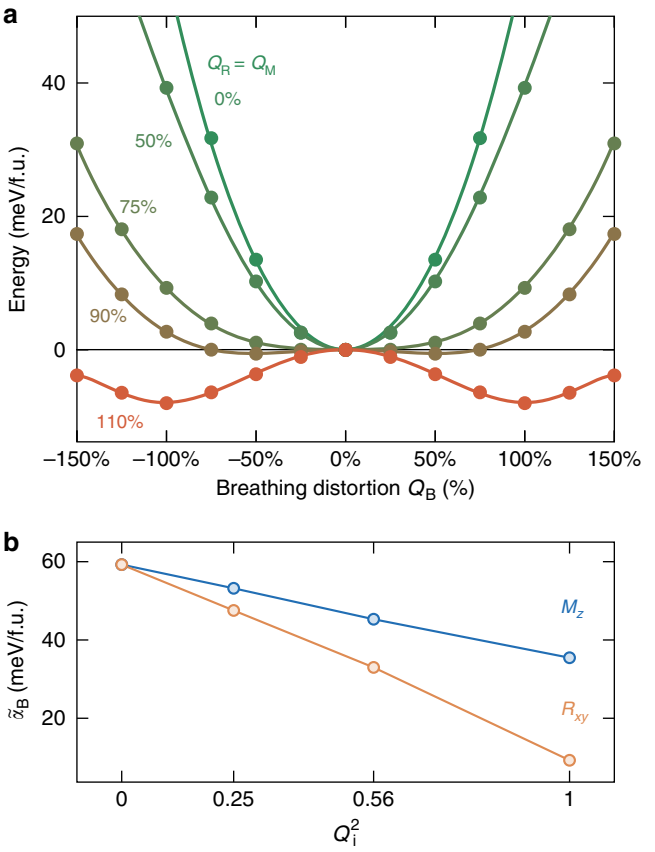

Fig. 2 Triggered mechanism. **a** Evolution of the energy E in terms of the amplitude of the breathing distortion (Q_B) for fixed amplitudes of oxygen rotations ($Q_R = Q_M$ from 0 to 110%) in the FM cubic cell of $YNiO_3$ (same volume as the ground state). It highlights the softening of the energy well associated to B_{OC}, triggered by the oxygen rotations R_{xy} and M_z. **b** Linear evolution of the energy curvature at the origin, $\tilde{\alpha}_B$ along Q_B, in terms of the square of the amplitude of the individual distortions Q_R (orange) and Q_M (blue)

Landau model and phase diagram. To further assess the relevance of such a triggered mechanism in nickelates, we built a Landau model, including R_{xy}, M_z, and B_{OC} degrees of freedom[24], restricting ourselves to lowest coupling terms and assuming temperature dependence of the oxygen rotations only:

$$\begin{aligned} E = \quad & \gamma_R(T - T_{0R})Q_R^2 + \beta_R Q_R^4 + \lambda_{BR} Q_B^2 Q_R^2 \\ + \quad & \gamma_M(T - T_{0M})Q_M^2 + \beta_M Q_M^4 + \lambda_{BM} Q_B^2 Q_M^2 \\ + \quad & \alpha_B Q_B^2 + \beta_B Q_B^4 + \lambda_{MR} Q_M^2 Q_R^2. \end{aligned} \qquad (1)$$

Within this model, R_{xy} and M_z appear at T_{0R} and T_{0M}, respectively. On cooling, they progressively develop within the *Pbnm* phase and renormalize the energy curvature α_B of B_{OC} as made clear when grouping the Q_B^2 terms in Eq. (1):

$$\tilde{\alpha}_B = \alpha_B + \lambda_{BM} Q_M^2 + \lambda_{BR} Q_R^2 \qquad (2)$$

When reaching a critical amplitude at which $\tilde{\alpha}_B = 0$, they trigger the appearance of B_{OC} and produce concurrent structural and metal-insulator phase transitions. The phase transition appears to be second order within this model, which is however too simple to be conclusive on this point (Supplementary Note 10).

All parameters and their evolution with R were directly fitted from first principles; only Curie temperatures were uniformly scaled to reproduce the experimental T_{MI} of $YNiO_3$ (Supplementary Note 8). The phase diagram of nickelates as predicted within this model is reported in Fig. 3. This figure demonstrates that the cooperative coupling of B_{OC} with R_{xy} and M_z is a key mechanism that, by itself, accounts for the experimentally observed evolution of T_{MI} with the tolerance factor.

Hence, the MIT in nickelates turns out to be a concrete example of triggered phase transition[26, 27], a kind of transition never identified before in simple perovskites. Indeed, although bi-quadratic interactions are generic in this class of compounds, different distortions usually compete and exclude each other[9]. The cooperative coupling of B_{OC} with oxygen rotations pointed out here is therefore an unusual and intriguing feature, whose origin is now traced back in the electronic band structure.

Electronic origin of the triggered mechanism. In the cubic phase, as expected from the formal Ni $3d^7\left(t_{2g}^6 e_g^1\right)$ occupancy, the Fermi energy E_f crosses levels of dominant Ni $3d$-e_g character (i.e., anti-bonding Ni $3d$-O $2p$ states); such levels form an isolated and rather dispersive set of two e_g bands, shifted above the t_{2g} levels by the crystal field (Fig. 4). Forcing into this cubic structure a B_{OC} distortion, associated to a phonon at $\mathbf{q}_R = (1/2, 1/2, 1/2)$, can open a gap at $\mathbf{q}_c = (1/4, 1/4, 1/4)$ within the e_g bands but well above E_f and without any direct impact on the metallic character and the occupied states. Nevertheless, the oxygen rotation motions substantially affect the e_g bands (Fig. 4), reducing their bandwidth and yielding a progressive down shift of the e_g levels at

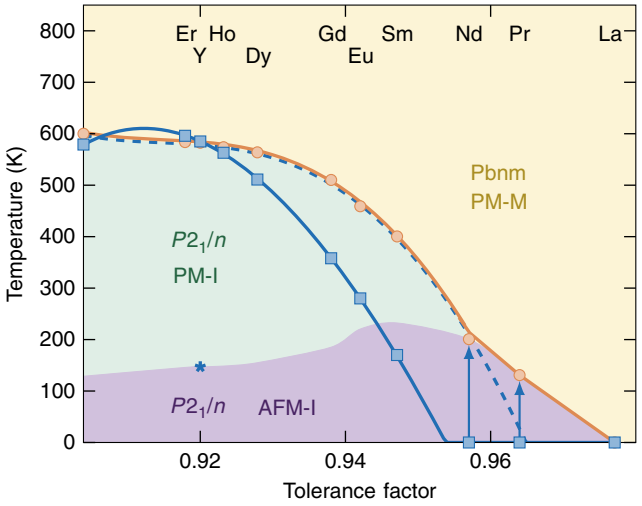

Fig. 3 Nickelate phase diagram. Phase diagram of $RNiO_3$ compounds in terms of their tolerance factor t and the temperature T. It includes three phases: a metallic *Pbnm* paramagnetic phase (PM-M, yellow area); an insulating $P2_1/n$ paramagnetic phase (PM-I, green area); and an insulating $P2_1/n$ E′-type AFM phase (AFM-I, magenta area). The yellow line and dots show the experimental evolution of T_{MI} with the tolerance factor t. The blue line and squares is the prediction of the simple Landau model fitted on the first-principles data (FM order). The dashed blue line is the fit of the Landau expression of T_{MI} (t) on experimental data. The blue star is the magnetic phase transition predicted for $YNiO_3$ from first principles. The blue arrows indicate the correction to be applied on T_{MI} for large cations when properly incorporating the change of magnetic order

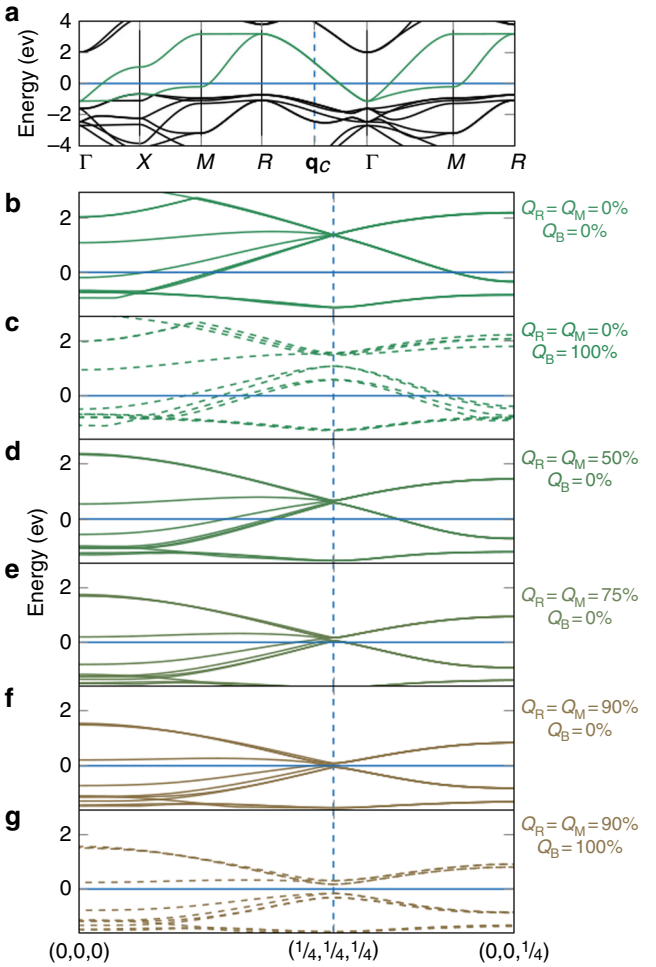

Fig. 4 Electronic properties. **a** Electronic dispersion curves of $YNiO_3$ along different high-symmetry line of the Brillouin zone of the $Pm\bar{3}m$ phase (FM case, majority spins): Γ = (0, 0, 0), X = (1/2, 0, 0), M = (1/2, 1/2, 0), and R = (1/2, 1/2, 1/2). The Ni 3d e_g bands are highlighted in green. The Fermi energy corresponds to the horizontal blue line. The point $\mathbf{q}_c$ = (1/4, 1/4, 1/4) is located by vertical dashed blue lines. **b**–**g** Electronic dispersion curves around the Fermi energy E_f (FM order, majority spins) along high-symmetry points (coordinates in pseudocubic notations) in the Brillouin zone of the *Pbnm* or $P2_1/n$ 20-atom cell, in which bands have been folded respect to **a**. Consecutive panels show the evolution of the dispersion curves when freezing into the $Pm\bar{3}m$ phase increasing amplitudes of oxygen rotations ($Q_R = Q_M =$ **b** 0%, **d** 50%, **e** 75%, or **f** 90%, lines) and eventually adding the breathing distortion (Q_B = 100% and $Q_R = Q_M =$ **c** 0% or **g** 90%, dashed lines)

$\mathbf{q}_c$. As the rotations gradually increase and the bandwidth decreases, B_{OC} more substantially pushes down the electronic states around E_f, providing a progressive gain of electronic energy, which, in turn, results in the softening of ω_B. The critical rotation amplitude at which B_{OC} becomes unstable ($\tilde{\alpha}_B = 0$) is precisely that at which the e_g levels at $\mathbf{q}_c$ cross E_f. At these amplitudes, the electronic system itself becomes unstable; the appearance of B_{OC} is favored and opens a gap at E_f, making the system insulating. As such, the MIT can therefore be interpreted as a Peierls instability but one that is not initially present and has been triggered by oxygen rotations.

Discussion

For compounds with small R cations, Q_R and Q_M are large and able to produce the MIT at relatively high temperatures, well above T_N. For large cations (R = Nd, Pr), oxygen rotations are reduced and, from our Landau model (built on FM results), no more sufficient to trigger the MIT (Fig. 3). However, as previously mentioned, the AFM-E′ spin order is compatible by symmetry with B_{OC} and induces its appearance as an improper order (linear shift of B_{OC} SW, Fig. 1d). Hence, although not opening a gap in the cubic phase, the onset of the AFM-E′ order in the *Pbnm* phase of $NdNiO_3$ and $PrNiO_3$ promotes the occurrence of the MIT almost triggered by the rotations. In these compounds, we have therefore $T_{MI} = T_N$; the transition is more abrupt and first-order[8]. Such active role of magnetism for large cations is supported by the experimental results and discussion in ref. [28]. It is also confirmed by our first-principles calculations on $NdNiO_3$, showing that the predicted T_{MI} is rescaled when including the change of magnetic order: while the system prefers to stay in the *Pbnm* metallic phase when imposing a FM order, it switches to the $P2_1/n$ phase when adopting a AFM-E′ order. The cooperative effect of the magnetic order remains true for small cations but without any impact on T_{MI} ($>T_N$).

In conclusion, the concurrent electronic and structural transitions at T_{MI} in $RNiO_3$ compounds take the form of a Peierls instability, which, primarily, is structurally triggered by the oxygen rotation motions R_{xy} and M_z and, eventually, is further assisted by the appearance of the E′-type AFM magnetic ordering. Our Landau model, and its possible extension to incorporate explicitly strain degrees of freedom neglected here for simplicity, provides a simple and useful quantitative tool to estimate and interpret how T_{MI} can be tuned toward the monitoring of oxygen rotation motions R_{xy} and M_z when making solid solutions[10], applying pressure[8], or playing with the epitaxial strain and the orientation of the substrate in thin films[29]. Our findings are relevant to other families of perovskites like A^{2+} Fe^{4+} O_3 compounds[30]. For instance, they can explain why $CaFeO_3$, which exhibits oxygen rotations, undergoes a MIT while $SrFeO_3$ and

$BaFeO_3$, which stay cubic, remain metallic. In addition, the same physics is also inherent to manganites like $LaMnO_3$, suggesting a close competition between charge and orbital orderings in this family compounds. However, the situation is slightly different in a bismutate like $BaBiO_3$, in which B_{OC} is intrinsically unstable in the cubic phase[31].

Methods

First-principles calculations. First-principles calculations were performed in the framework of DFT[32, 33] using a Projected Augmented Wave (PAW) approach[34] as implemented within the ABINIT package[35–38]. The calculations relied on the Generalized Gradient Approximation using the PBEsol[39] exchange-correlation functional. We worked within a collinear spin approximation. We included a Hubbard correction $U = 1.5$ eV[40] on the 3*d* orbitals of Ni atoms. A special care was devoted to the determination of the appropriate *U* parameter (Supplementary Notes 1–4).

We made use of JTH atomic potentials[41]. For the wavefunctions, we used an energy cutoff of 24 Ha (38 Ha for the second grid in the PAW spheres), which guarantees a convergence better than 1 meV on the total energy. The BZ was sampled with *k*-point meshes equivalent to a $12 \times 12 \times 12$ grid in the five-atom unit cell. During structural relaxations, thresholds of 10^{-5} Ha/bohr on the maximum force and of 10^{-7} Ha/bohr^3 on the maximum stress have been considered.

Structural analysis. The Goldschmidt tolerance factor[42], $t = d_{R-O}/\sqrt{2}d_{Ni-O}$, of $RNiO_3$ compounds were determined using Nicole Benedek's tool[43] relying on a bond valence model[44] to calculate d_{R-O} and d_{Ni-O}, respectively, the ideal *R*–O and Ni–O bond lengths in the cubic perovskite structure.

Symmetry-adapted mode analysis have been performed with AMPLIMODE[45, 46]. The modes are normalized to their amplitude in the $P2_1/n$ AFM-E′ ground state. This normalization is such that in cubic phase (volume of the ground state) $Q_R = 100\%$ corresponds to rotation angles $\phi_x = \phi_y = 11.33°$ (Ni–O–Ni angle of 157.33°), $Q_R = 100\%$ corresponds to a rotation angle $\phi_z = 12.12°$ (Ni–O–Ni angle of 155.75°) and $Q_B = 100\%$ corresponds to oxygen displacements $d_O = 0.0358$.

Landau model. The Landau model parameters have been fitted for $YNiO_3$, $GdNiO_3$, and $SmNiO_3$ on first-principles data using in each case a FM cubic phase (volume of the ground state) and interpolated for the other compounds. T_{MI} was determined analytically (Supplementary Notes 6–9).

Data availability. All relevant data are available from the authors.

Received: 11 September 2017 Accepted: 15 October 2017
Published online: 22 November 2017

References

1. Demazeau, G., Marbeuf, A., Pouchard, M. & Hagenmuller, P. Sur une série de composés oxygènes du nickel trivalent derivés de la perovskite. *J. Solid State Chem.* **3**, 582 (1971).
2. Shi, J., Ha, S. D., Zhou, Y., Schoofs, F. & Ramanathan, S. A correlated nickelate synaptic transistor. *Nat. Commun.* **4**, 2676 (2013).
3. Zhou, Y. et al. Strongly correlated perovskite fuel cells. *Nature* **534**, 231–234 (2016).
4. Middey, S. et al. Physics of ultrathin films and heterostructures of rare-earth nickelates. *Annu. Rev. Mater. Res.* **46**, 305–334 (2016).
5. Först, M. et al. Spatially resolved ultrafast magnetic dynamics initiated at a complex oxide heterointerface. *Nat. Mater.* **14**, 883–888 (2015).
6. Kim, T. H. et al. Polar metals by geometric design. *Nature* **533**, 68–72 (2016).
7. Grisolia, M. N. et al. Hybridization-controlled charge transfer and induced magnetism at correlated oxide interfaces. *Nat. Phys.* **12**, 484–492 (2016).
8. Catalan, G. Progress in perovskite nickelate research. *Phase Transit.* **81**, 729–749 (2008).
9. Benedek, N. A. & Fennie, C. J. Why are there so few perovskite ferroelectrics? *J. Phys. Chem. C* **117**, 13339–13349 (2013).
10. Medarde, M. L. Structural, magnetic and electronic properties of $RNiO_3$ perovskites (R = rare earth). *J. Phys. Condens. Matter* **9**, 1679 (1997).
11. Alonso, J. A. et al. Charge disproportionation in *RniO*$_3$ perovskites: simultaneous metal-insulator and structural transition in *YNiO*$_3$. *Phys. Rev. Lett.* **82**, 3871–3874 (1999).
12. García-Muñoz, J. L., Rodríguez-Carvajal, J. & Lacorre, P. Neutron-diffraction study of the magnetic ordering in the insulating regime of the perovskites $RNiO_3$ R = Pr and Nd). *Phys. Rev. B* **50**, 978–992 (1994).
13. Lee, S., Chen, R. & Balents, L. Landau theory of charge and spin ordering in the nickelates. *Phys. Rev. Lett.* **106**, 016405 (2011).
14. Torrance, J. B., Lacorre, P., Nazzal, A. I., Ansaldo, E. J. & Niedermayer, C. Systematic study of insulator-metal transitions in perovskites $RniO_3$ R = Pr, Nd, Sm, Eu) due to closing of charge-transfer gap. *Phys. Rev. B* **45**, 8209–8212 (1992).
15. Mizokawa, T., Khomskii, D. I. & Sawatzky, G. A. Spin and charge ordering in self-doped Mott insulators. *Phys. Rev. B* **61**, 11263–11266 (2000).
16. Raebiger, H., Lany, S. & Zunger, A. Charge self-regulation upon changing the oxidation state of transition metals in insulators. *Nature* **453**, 763–766 (2008).
17. Park, H., Millis, A. J. & Marianetti, C. A. Site-selective mott transition in rare-earth-element nickelates. *Phys. Rev. Lett.* **109**, 156402 (2012).
18. Ruppen, J. et al. Optical spectroscopy and the nature of the insulating state of rare-earth nickelates. *Phys. Rev. B* **92**, 155145 (2015).
19. Varignon, J., Grisolia, M. N., Iniguez, J., Barthélémy, A. & Bibes, M. Complete phase diagram of rare-earth nickelates from first principles. *npj Quant. Mater.* **2**, 21 (2017).
20. Mazin, I. I. et al. Charge ordering as alternative to jahn-teller distortion. *Phys. Rev. Lett.* **98**, 176406 (2007).
21. Johnston, S., Mukherjee, A., Elfimov, I., Berciu, M. & Sawatzky, G. A. Charge disproportionation without charge transfer in the rare-earth-element nickelates as a possible mechanism for the metal-insulator transition. *Phys. Rev. Lett.* **112**, 106404 (2014).
22. Bisogni, V. et al. Ground state oxygen holes and the metal-insulator transition in the negative charge transfer rare-earth nickelates. *Nat. Commun.* **7**, 13017 (2016).
23. de la Cruz, F. P. et al. Possible common ground for the metal-insulator phase transition in the rare-earth nickelates $RniO_3$ (R = Eu, Ho, Y). *Phys. Rev. B* **66**, 153104 (2002).
24. Balachandran, P. V. & Rondinelli, J. M. Interplay of octahedral rotations and breathing distortions in charge-ordering perovskite oxides. *Phys. Rev. B* **88**, 054101 (2013).
25. Holakovsky, J. A new type of ferroelectric phase transition. *Phys. Status Solidi B* **56**, 615–619 (1973).
26. Flerov, I. N., Gorev, M. V., Voronov, V. N., Tressaud, A. & Grannec, J. Triggered phase transitions in $Rb_2KB^{3+}F_6(B^{3+}$: Er, ho) elpasolites. *J. Solid State Chem.* **3**, 582 (1971).
27. Iwata, M., Zhao, C. H., Aoyagi, R., Maeda, M. & Ishibashi, Y. Splitting of triggered phase transition in $Bi_{4-x}La_xTi_3O_{12}$ mixed crystals. Japonese. *J. Appl. Phys.* **46**, 5894 (2007).
28. Vobornik, I. et al. Electronic-structure evolution through the metal-insulator transition in $RniO_3$. *Phys. Rev. B* **60**, R8426–R8429 (1999).
29. Catalano, S. et al. Tailoring the electronic transitions of $NdNiO_3$ films through (111)pc oriented interfaces. *APL Mater.* **3**, 062506 (2015).
30. Akao, T. et al. Charge-ordered state in single-crystalline $CaFeO_3$ thin film studied by x-ray anomalous diffraction. *Phys. Rev. Lett.* **91**, 156405 (2003).
31. Liechtenstein, A. I. et al. Structural phase diagram and electron-phonon interaction in $Ba_{1-x}K_xBiO_3$. *Phys. Rev. B* **44**, 5388–5391 (1991).
32. Hohenberg, P. & Kohn, W. Inhomogeneous electron gas. *Phys. Rev.* **136**, B864–B871 (1964).
33. Kohn, W. & Sham, L. J. Self-consistent equations including exchange and correlation effects. *Phys. Rev.* **140**, A1133–A1138 (1965).
34. Blöchl, P. E. Projector augmented-wave method. *Phys. Rev. B* **50**, 17953–17979 (1994).
35. Gonze, X. et al. ABINIT: First-principles approach to material and nanosystem properties. *Comput. Phys. Commun.* **180**, 2582–2615 (2009).
36. Gonze, X. et al. First-principles computation of material properties: the ABINIT software project. *Computat. Mater. Sci.* **25**, 478–492 (2002).
37. Gonze, X. et al. A brief introduction to the abinit software package. *Z. Kristallogr. Cryst. Mater.* **220**, 558–562 (2005).
38. Torrent, M., Jollet, F., Bottin, F., Zérah, G. & Gonze, X. Implementation of the projector augmented-wave method in the ABINIT code: application to the study of iron under pressure. *Comput. Mater. Sci.* **42**, 337–351 (2008).
39. Perdew, J. P. et al. Restoring the density-gradient expansion for exchange in solids and surfaces. *Phys. Rev. Lett.* **100**, 136406 (2008).
40. Liechtenstein, A. I., Anisimov, V. I. & Zaanen, J. Density-functional theory and strong interactions: orbital ordering in mott-hubbard insulators. *Phys. Rev. B* **52**, R5467–R5470 (1995).
41. Jollet, F., Torrent, M. & Holzwarth, N. Generation of Projector Augmented-Wave atomic data: a 71 element validated table in the XML format. *Comput. Phys. Commun.* **185**, 1246–1254 (2014).
42. Goldschmidt, V. M. Die gesetze der krystallochemie. *Naturwissenschaften* **14**, 477–485 (1926).
43. Benedek, N. Tolerance factor calculator v0.2.1.
44. Lufaso, M. W. & Woodward, P. M. Prediction of the crystal structures of perovskites using the software program spuds. *Acta. Crystallogr. B.* **57**, 725 (2001).
45. Orobengoa, D., Capillas, C., Aroyo, M. I. & Perez-Mato, J. M. AMPLIMODES: symmetry-mode analysis on the Bilbao Crystallographic Server. *J. Appl. Crystallogr.* **42**, 820–833 (2009).
46. Perez-Mato, J. M., Orobengoa, D. & Aroyo, M. I. Mode crystallography of distorted structures. *Acta Crystallogr. A* **66**, 558–590 (2010).

Acknowledgements

We thank Y. Zhang, E. Bousquet, F. Ricci, M. Verstraete, J.-Y. Raty, S. Catalano, J.-M. Triscone, A. Georges and J. Varignon for fruitful discussions. This work was supported by FRS-FNRS project HiT4FiT and ARC project AIMED. J.I. acknowledges support form FNR Luxembourg Grant P12/4853155 "COFERMAT". Calculations have been performed on the Céci facilities funded by F.R.S-FNRS (Grant No 2.5020.1) and Tier-1 supercomputer of the Fédération Wallonie-Bruxelles funded by the Walloon Region (Grant No 1117545). They also took advantage of HPC resources from the French Research and Technology Computing Center (CCRT) and from the PRACE project Megapasta.

Author contributions

P.G. conceived the study with A.M. and J.I. and directed the work. A.M. and J.B. did the first-principles simulations. A.M. and P.G. did the Landau modeling. P.G. wrote the manuscript with A.M. and J.B. All authors discussed the results at different stages of the study and commented on the manuscript.

Additional information

Supplementary Information accompanies this paper at doi:10.1038/s41467-017-01811-x.

Competing interests: The authors declare no competing financial interests.